

## Article

# Catalytic Performance of Bimetallic Cobalt–Nickel/Graphene Oxide for Carbon Dioxide Reforming of Methane

Sharifah Nur Sorfina Syed Abu Bakar<sup>1</sup>, May Ali Alsaffar<sup>2</sup>, Bawadi Abdullah<sup>1</sup>, Maizatul Shima Shaharun<sup>3,4</sup>, Sureena Abdullah<sup>5</sup>  and Bamidele Victor Ayodele<sup>1,3,\*</sup> 

<sup>1</sup> Department of Chemical Engineering, Universiti Teknologi PETRONAS, Bandar Seri Iskandar 32610, Perak, Malaysia; sharifah\_18002260@utp.edu.my (S.N.S.S.A.B.); bawadi\_abdullah@utp.edu.my (B.A.)

<sup>2</sup> Department of Chemical Engineering, University of Technology-Iraq, Baghdad 10066, Iraq; mayrashid1973@gmail.com

<sup>3</sup> CO<sub>2</sub> Research Center (CO<sub>2</sub>RES), Institute of Contaminant Management, Universiti Teknologi PETRONAS, Bandar Seri Iskandar 32610, Perak, Malaysia; maizats@utp.edu.my

<sup>4</sup> Department of Fundamental and Applied Science, Universiti Teknologi PETRONAS, Bandar Seri Iskandar 32610, Perak, Malaysia

<sup>5</sup> Faculty of Chemical and Process Engineering Technology, College of Engineering Technology, Universiti Malaysia Pahang Al-Sultan Abdullah, Gambang-Kuantan 26300, Pahang, Malaysia; sureena@ump.edu.my

\* Correspondence: ayodelevb@gmail.com or bamidele.ayodele@utp.edu.my

**Abstract:** The design of economical and robust catalysts is a substantial challenge for the dry reforming of methane (DRM). Monometallic nickel-based catalysts used for DRM reactions had comparable activity to noble metals. However, they turned out to be less stable during the reactions. As a continuation of the interest in synthesizing catalysts for DRM, this paper evaluates the catalytic performance of bimetallic Co–Ni catalysts regarding their synergy effect, with graphene oxide (GO) as support for the first time. The synthesized bimetallic catalysts prepared via the wet-impregnation method were characterized using N<sub>2</sub> physisorption analysis, scanning electron microscopy (SEM), thermogravimetric analysis (TGA), and X-ray diffraction (XRD). The catalytic test was performed in a stainless-steel tubular reactor in atmospheric conditions with a reaction temperature of 800 °C, time-on-stream (TOS) of 300 min and CH<sub>4</sub>: CO<sub>2</sub> being fed with a ratio of 1:1. The bimetallic 10 wt%Co–10 wt%Ni/GO and 20 wt%Co–10 wt%Ni/GO catalysts had a similar BET specific surface area in N<sub>2</sub> physisorption analysis. The XRD pattern displayed a homogeneous distribution of the Co and Ni on the GO support, which was further validated through SEM–EDX. The conversion of CO<sub>2</sub>, CH<sub>4</sub>, and H<sub>2</sub> yield decreased with reaction time due to the massive occurrence of side reactions. High conversions for CO<sub>2</sub> and CH<sub>4</sub> were 94.26% and 95.24%, respectively, attained by the bimetallic 20 wt%Co–10 wt%Ni/GO catalyst after 300 min TOS, meaning it displayed the best performance in terms of activity among all the tested catalysts.

**Keywords:** cobalt; dry reforming of methane; graphene oxide; nickel; hydrogen-rich syngas



**Citation:** Bakar, S.N.S.S.A.; Alsaffar, M.A.; Abdullah, B.; Shaharun, M.S.; Abdullah, S.; Ayodele, B.V. Catalytic Performance of Bimetallic Cobalt–Nickel/Graphene Oxide for Carbon Dioxide Reforming of Methane. *ChemEngineering* **2023**, *7*, 107. <https://doi.org/10.3390/chemengineering7060107>

Academic Editor: Dmitry Yu. Murzin

Received: 5 October 2023

Revised: 24 October 2023

Accepted: 2 November 2023

Published: 7 November 2023



**Copyright:** © 2023 by the authors. Licensee MDPI, Basel, Switzerland. This article is an open access article distributed under the terms and conditions of the Creative Commons Attribution (CC BY) license (<https://creativecommons.org/licenses/by/4.0/>).

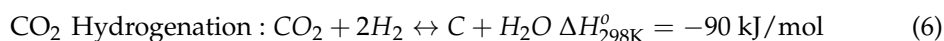
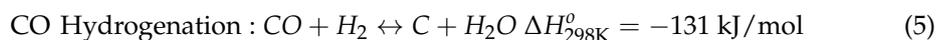
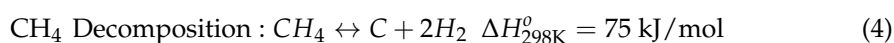
## 1. Introduction

Greenhouse gases that are being emitted excessively, such as carbon dioxide (CO<sub>2</sub>), methane (CH<sub>4</sub>) and nitrous oxide (N<sub>2</sub>O), have led to concern about climate change and environmental pollution [1]. Hence, many efforts are being made to mitigate the detrimental effects caused by the emissions of these gases [2,3]. Among all the emissions, CO<sub>2</sub> is identified to be the most abundant anthropogenic greenhouse gas (GHG), followed by CH<sub>4</sub>. In view of this, converting these gases into beneficial and valuable feedstock reduces the emission of CO<sub>2</sub> and CH<sub>4</sub> into the atmosphere with the potential for producing a wide range of materials and useful chemicals [4]. The CO<sub>2</sub> reforming of CH<sub>4</sub>, generally referred to as the dry reforming of methane (DRM), is one of the alternative reactions for CH<sub>4</sub>,

reforming it to generate syngas [5]. Owing to this, DRM provides a promising way to alleviate the greenhouse effects and is said to be of great experimental interest. It is also preferable in comparison to the other three processes, namely steam reforming of CH<sub>4</sub> (SRM), partial oxidation of CH<sub>4</sub> (POM), and the combination of these two methods, the auto-thermal reforming of CH<sub>4</sub> (ATRM).



The consumption of GHGs in DRM, where CO<sub>2</sub> reacts with CH<sub>4</sub> to generate syngas that consists of carbon monoxide (CO) and hydrogen (H<sub>2</sub>), is depicted in Equation (1). According to Summa, Samojeden, and Motak [6], CH<sub>4</sub> plays the role of a reducing agent while CO<sub>2</sub> is an oxidant. As such, this method contributes to CO<sub>2</sub> mitigation and is applicable to gases containing both CO<sub>2</sub> and CH<sub>4</sub>, for instance, biogas. The products generated in Equation (1) are crucial raw materials for the synthesis of oxygenated chemicals and long-chain hydrocarbons in the Fischer–Tropsch industry [7]. Furthermore, H<sub>2</sub>, as one of the products, is a vital source of clean fuel that can significantly reduce the impact of greenhouse emissions [8]. For decades, H<sub>2</sub> has been dominating industry, especially in oil refining and the production of ammonia, as a fundamental raw material [9]. Apart from the desired reaction, several side reactions can occur simultaneously during the process. Among the common side reactions is the reverse water gas reaction (RWGS) resulting from the operating conditions in which water is produced, as shown in Equation (2) [10]. From the perspective of applied catalysis, the non-desired reactions lead to coke formation during the process [11]. The CO disproportionation is defined as the Boudouard reaction, presented in Equation (3). Meanwhile, the complete decomposition of CH<sub>4</sub> toward solid carbon over the catalytic surface and emission of H<sub>2</sub> occurs in CH<sub>4</sub> decomposition, shown in Equation (4) [12]. Additionally, catalyst deactivation can be accelerated by the reduction of CO and CO<sub>2</sub> toward carbon, as shown in Equations (5) and (6), respectively, which occur in parallel [13].



Previous studies explored the performance of noble and non-noble metals as DRM catalysts [14,15]. In the context of supported noble metals, they are found to be highly active and selective towards the production of syngas, with the following activity orders typically observed: Rh > Ru > Pd > Ir~Pt [16]. Generally, each study has resulted in the same output, where the authors have agreed that the higher catalytic activity for CH<sub>4</sub> and CO<sub>2</sub> conversion is attained by noble metals from groups X, for instance, ruthenium (Ru) [17], rhodium (Rh) [18], iridium (Ir) [19], palladium (Pd) [20], and platinum (Pt) [21] due to excellent resistance to carbon formation in contrast to non-noble metals. Nonetheless, their utilization on a large scale is hindered by high costs and insufficient resources [22]. For this reason, research in DRM focusing on designing a high-activity and feasible catalyst based on non-noble metals has been a topic of interest in recent years, especially cheap transition-metal-based catalysts such as nickel (Ni) and cobalt (Co).

Despite comparable performance displayed by Ni to noble metal catalysts in DRM reaction, its deactivation remains a barrier when selecting robust catalyst [11,23]. In contrast,

Co is more stable compared to Ni during the DRM reaction but displayed a lower catalytic activity. Hence, the coupling of Co and Ni can potentially enhance the catalytic performance of DRM on the grounds of surface structure modification [24–26]. The synergistic effects of this bimetallic catalyst were extensively reported by numerous studies.

Although monometallic Co catalyst is prone to oxidation caused by high affinity for oxygen species, this attribute rarely impacts the catalytic performance of bimetallic Ni–Co catalyst. Moreover, the high oxygen affinity possessed by Co could help to minimize its deactivation. This could be achieved by suppressing the coke formation through oxidation, as depicted in the reverse Boudouard reaction [27]. The synergistic effects of using both Ni and Co in DRM could help to enhance the catalytic activity [28]. Accordingly, the rate of CH<sub>4</sub> dehydrogenation can be reduced significantly by Co, which is less active than Ni in CH<sub>4</sub> cracking. Over the years, several studies on representative bimetallic Co–Ni catalysts on various supports have been extensively reported. To the best of the authors' knowledge, there is a dearth of studies on the application of GO as a support for bimetallic Co–Ni catalysts used for DRM reactions. Studies have shown that the use of GO support for a metal-organic framework (MOF) catalyst gives a high dispersion of nanoparticles [29]. Therefore, this study aims to investigate the catalytic performance of GO-supported bimetallic Co–Ni catalysts as a concept to steer its catalytic activity in DRM reactions.

## 2. Materials and Methods

### 2.1. Materials

The precursors used for the synthesis of the Co–Ni catalysts include nickel (II) nitrate hexahydrate (Ni (NO<sub>3</sub>)<sub>2</sub>·6H<sub>2</sub>O) and cobalt (II) nitrate hexahydrate (Co (NO<sub>3</sub>)<sub>2</sub>·6H<sub>2</sub>O). GO was used as the support. The Ni (NO<sub>3</sub>)<sub>2</sub>·6H<sub>2</sub>O and Co (NO<sub>3</sub>)<sub>2</sub>·6H<sub>2</sub>O were purchased from Sigma–Aldrich, (St. Louis, MI, USA). GO was purchased locally. All the materials were analytical grade and used without further purification.

### 2.2. Catalyst Preparation

The GO-supported bimetallic Co–Ni catalysts were synthesized via the wet-impregnation method. The Ni (NO<sub>3</sub>)<sub>2</sub>·6H<sub>2</sub>O (purity: >97%, Sigma–Aldrich, CAS: 13478-00-7) and Co(NO<sub>3</sub>)<sub>2</sub>·6H<sub>2</sub>O (purity: >98%, Sigma–Aldrich, CAS: 10026-22-9) were used as Ni and Co active metal phase precursors, respectively. The Co–Ni/GO catalysts were prepared by impregnating the Ni(NO<sub>3</sub>)<sub>2</sub>·6H<sub>2</sub>O and Co(NO<sub>3</sub>)<sub>2</sub>·6H<sub>2</sub>O salt solution into the GO support, followed immediately by magnetic stirring for 24 h. The mixture was then dried overnight in an oven at 60 °C and calcined in a muffle furnace under an air atmosphere at 650 °C for 4 h. Three different sets of the Co–Ni/GO catalysts were prepared by varying the weight loading of the Ni and Co between 10 wt% and 20 wt%, as depicted in Table 1.

**Table 1.** Metal and support content of the bimetallic catalysts.

Catalyst	Co (wt%)	Ni (wt%)	Total Metal (wt%)
1Co–1Ni/GO	10	10	20
1Co–2Ni/GO	10	20	30
2Co–1Ni/GO	20	10	30

### 2.3. Catalyst Characterization

The freshly calcined catalysts were characterized using N<sub>2</sub> adsorption–desorption analysis, scanning electron microscopy (SEM), energy dispersive X-ray (EDX), thermogravimetric analysis (TGA), and X-ray diffraction (XRD).

The BET surface area, pore volume, and pore diameter of the freshly synthesized catalysts were measured by the N<sub>2</sub> physisorption method at –196 °C using a Micromeritics ASAP 2020 surface and porosity analyzer. Prior to the measurements, the synthesized catalyst samples were degassed at 300 °C to remove the moisture and other adsorbed gases from the surface. The specific surface area of the catalysts was calculated by the BET

equation, while the pore diameter was calculated using the Barrett, Joyner, and Halenda (BJH) method.

The surface morphology of the freshly synthesized catalysts and their elemental compositions were examined using SEM on a Zeis EVO LS 15 equipped with EDX. Prior to the analysis, the catalyst samples were coated to improve imaging. Subsequently, the catalyst samples were mounted on standard specimen stubs assisted by double adhesive carbon tape. The SEM machine was operated at an accelerating electron volt of 25 keV and a 3 nA beam current.

The thermal properties of the freshly synthesized catalysts as a function of temperature were analyzed prior to calcination using TGA on a Perkin Elmer Simultaneous Thermal Analyzer (STA) 6000. The uncalcined fresh catalysts were heated in air from 30 °C to 900 °C at a ramping rate of 10 °C/min.

XRD analysis was conducted on the freshly synthesized catalysts to examine their crystallinity. The recording of the XRD diffractogram was carried out using a Malvern Panalytical Xpert3 Powder. Diffraction peaks were recorded in a 2θ range of 10° to 90° at a scanning rate of 6°/min with an X-ray source of Cu Kα at 0.154 nm radiation in wavelength (λ).

The catalyst activities were evaluated in the DRM reaction using a fixed-bed continuous reactor with an inner diameter of 10 mm and a length of 35 cm (Figure 1). The DRM reaction was initiated at 800 °C for 5 h time-on-stream (TOS) under atmospheric pressure. The catalyst, weighing 150 mg, was supported with quartz wool at the center of the fixed-bed reactor mounted vertically in a furnace equipped with a Type-K thermocouple and proportional integral derivative (PID) temperature controller. Prior to testing, the catalysts were reduced in situ in a flow of 60 mL/min H<sub>2</sub>/N<sub>2</sub> (1:1) at 850 °C for 1 h to reduce the metal oxide into the active metal. Subsequently, the reactor was purged in a flow of N<sub>2</sub> for 30 min. The catalytic evaluation was performed by feeding CH<sub>4</sub> (20 mL/min), CO<sub>2</sub> (20 mL/min), and N<sub>2</sub> (20 mL/min) gas flow into the reactor at a stoichiometric feed ratio of 1:1:1. Agilent 4890 gas chromatography with N<sub>2</sub> as the carrier gas and a temperature-controlled detector (TCD) was employed to determine the composition of the exit gaseous product. As depicted in Equations (7)–(9), catalytic performance was evaluated in terms of reactant conversions, as well as H<sub>2</sub> yield.

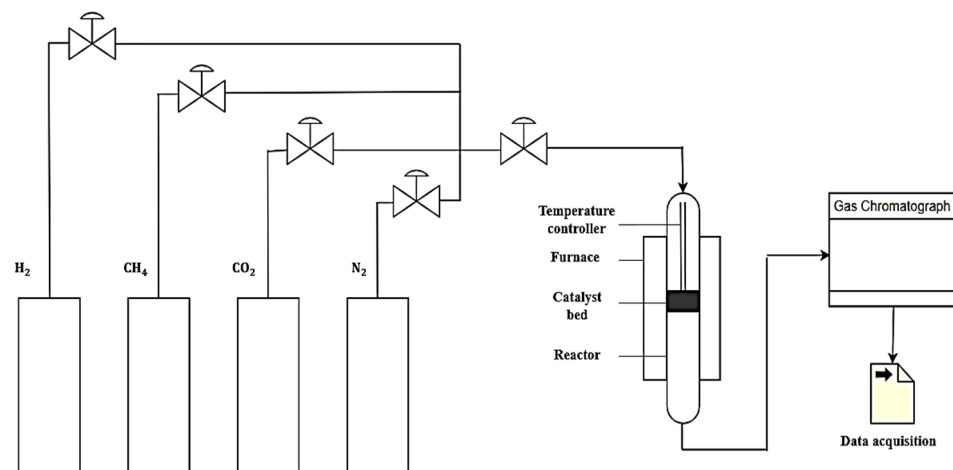


**Figure 1.** Schematic diagram showing the experimental setup for the catalyst testing in the DRM reaction.

$$\text{CH}_4 \text{ conversion : } X_{\text{CH}_4} = \frac{F_{\text{CH}_4, \text{in}} - F_{\text{CH}_4, \text{out}}}{F_{\text{CH}_4, \text{in}}} \times 100\% \quad (7)$$

$$\text{CO}_2 \text{ conversion : } X_{\text{CO}_2} = \frac{F_{\text{CO}_2, \text{in}} - F_{\text{CO}_2, \text{out}}}{F_{\text{CO}_2, \text{in}}} \times 100\% \quad (8)$$

$$\text{H}_2 \text{ yield} : Y_{\text{H}_2} = \frac{F_{\text{H}_2, \text{out}}}{2 \times F_{\text{CH}_4, \text{in}}} \quad (9)$$

where  $F_{i, \text{in}}$  and  $F_{i, \text{out}}$  are the molar flow rates of species  $i$  at the reactor inlet and outlet, respectively.

### 3. Results and Discussion

#### 3.1. Catalysts Characterization

Figure 2 represents the  $\text{N}_2$  adsorption–desorption isotherms and pore diameter differential distribution of the freshly synthesized bimetallic catalysts after 4 h of calcination at  $650^\circ\text{C}$ . The  $\text{N}_2$  adsorption–desorption isotherms obtained for all the catalysts showed a sharp increase after  $P/P_0 = 0.70$  in the second half of the isotherm. Such curves conformed to Type IV adsorption isotherm defined by IUPAC with an H3 hysteresis loop. This is an indication that the catalytic materials are mesoporous in nature [30].

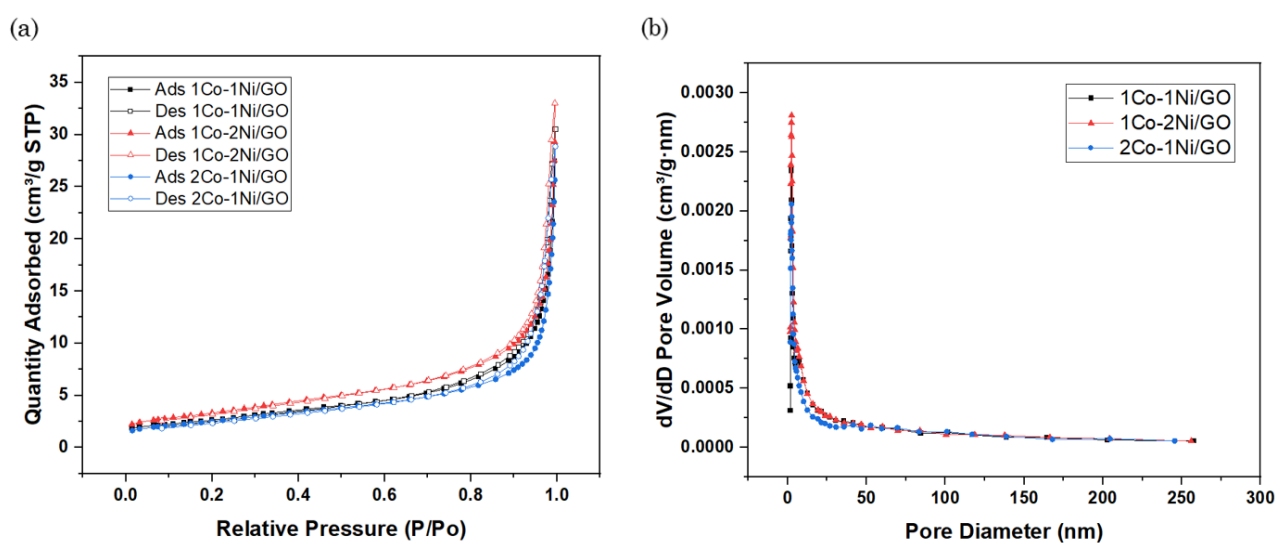


**Figure 2.** (a)  $\text{N}_2$  adsorption–desorption isotherms and (b) pore diameter distribution of the fresh catalysts.

The textural properties of the catalysts are summarized in Table 2. The calculation of the specific surface area and pore distributions of the catalysts using BET and BJH methods revealed that the 1Co–1Ni/GO catalyst exhibited considerably high surface area and large pore volume compared to the other catalysts. The particle diameter of the 1Co–1Ni/GO, 1Co–2Ni/GO, and 2Co–1Ni/GO were calculated as 16.4505 nm, 14.1692 nm, and 15.9061 nm, respectively. It can be seen that the 1Co–1Ni/GO and 2Co–1Ni/GO catalysts have almost the same BET surface area of  $\sim 9 \text{ m}^2/\text{g}$ , and 1Co–2Ni/GO obviously exhibited the largest surface area of  $12.0215 \text{ m}^2/\text{g}$  but with the lowest pore diameter. It seemed that the composition of the metals had an important effect on both the surface area and the pore diameter of the bimetallic catalyst. Generally, catalysts often display high specific surface areas with small metal grain sizes [31]. The textural properties of the catalysts obtained in this study indicate that the specific surface area of the bimetallic Co–Ni catalysts increases as the Ni loading increases. The Co and Ni nanoparticles were dispersed on the surface of the catalyst for the initiation of the DRM reaction [32]. Also, increasing the loading of the Co could result in a decline in total surface area and pore volume, which is consistent with the study reported in [33].

The SEM images depicted in Figure 3 were employed to examine the morphology of the freshly synthesized bimetallic Co–Ni/GO catalysts. The SEM micrograph of the catalysts at  $7000\times$  magnifications is depicted in Figure 3. Typically, GO had been reported to have a sponge-like morphology and raging formation with graphene sheets covered with porous carbon [34]. Studies have shown that GO shows a crumpled and wrinkled graphene sheet structure due to the deformation upon the exfoliation and restacking process, whereby the

morphology resembles a thin curtain [35]. These described characteristics can be observed in Figure 3a. Also, it can be clearly seen that the 2Ni-1Co/GO and 1Ni-2Co/GO catalysts displayed better homogeneous distribution of Co and Ni species on the surface than the 1Co-1Ni/GO catalyst. This could be attributed to the different loading of the GO as support in the three catalysts. The morphology of the catalysts changed from plate-like and flake-like at high GO support of 80 wt% to needle-like at low GO support of 70 wt% (Figure 3b,c). Furthermore, the SEM images of all catalysts displayed the formation of irregular and quite bulky surface morphology. The GO species seemed to exist as an adsorbed layer on the external surface of crystallites in the darker regions of SEM images. The catalyst particles showed a slight agglomeration of crystallites, associated with high calcination temperatures up to 650 °C [36]. As shown in Figure 4, all the stipulated elemental compositions of the Co-Ni/GO catalysts are captured by the EDX profile.

**Table 2.** Textural properties of the fresh catalysts.

Catalyst	$A_{BET}$ (m <sup>2</sup> /g) <sup>a</sup>	$V_p$ (cm <sup>3</sup> /g) <sup>b</sup>	$\bar{A}$ (nm) <sup>c</sup>
1Co-1Ni/GO	9.5921	0.0396	16.4504
1Co-2Ni/GO	12.0215	0.0427	14.1692
2Co-1Ni/GO	9.1568	0.0362	15.9061

<sup>a</sup> Surface area calculated by BET, <sup>b</sup> Pore volume calculated by BJH, <sup>c</sup> Average pore diameter (4 V/A by BET).

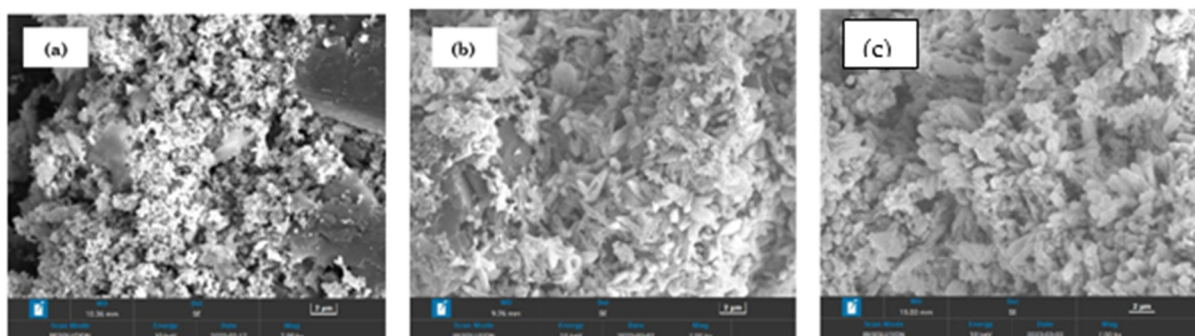


**Figure 3.** SEM images of the fresh (a) 1Co-1Ni/GO; (b) 1Co-2Ni/GO; (c) 2Co-1Ni/GO at 7000× magnification.

The TG analysis of the bimetallic Co-Ni/GO catalysts provided information on the weight loss and thermal stability of the uncalcined samples as a function of temperature increase from 30 °C to 900 °C. The thermal stability of the catalysts in inert nitrogen is represented in the TG curves and DTG profiles in Figure 5. Based on the TG curves, the decrease in weight as the temperature increases could be explained by the continuous change in the weight of the catalyst samples due to thermal treatment. All three catalysts exhibited three weight losses on the TG curves with increasing temperatures. For the 1Co-1Ni/GO catalyst, the first weight loss accounted for 20.40%, which occurred in a temperature range of 30 °C to 170 °C (stage I) and can be attributed to water removal through evaporation. Subsequently, the weight loss of 15.91% indicated the decomposition of nitrate salts to obtain the oxide of Co and Ni between 225 °C and 300 °C (Stage II). The final gradual weight loss of around 4.45% revealed the occurrence of exothermic combustion of GO at the range of 660 °C to 670 °C [18,21] (Stage III).

The weight loss for the 1Co-2Ni/GO and 2Co-1Ni/GO catalysts was higher than the 1Co-1Ni/GO catalyst due to faster dehydration, which accounts for ~27%. Despite similar drying conditions, the amount of adsorbed water was reduced for the 1Co-1Ni/GO catalyst. Taratayko, Kolobova, and Mamontov [21] suggested that catalysts with such properties had a more hydrophobic character. Also, the second step of weight loss in 1Co-2Ni/GO and 2Co-1Ni/GO resulted in 19.10% and 20.93%. This can be associated with higher total metal content in these two catalysts compared to 1Co-1Ni/GO. Thus, the weight loss for the decomposition of nitrate salts was slightly higher. It should be noted

that, with the increasing amount of Co in the precursors, a pronounced peak of weight loss appeared at 800 °C. By contrast, increasing the amount of Ni loading showed a slight increase in weight loss at 800 °C. Nevertheless, this occurrence in DTG curves was ascribed to the reaction of the produced carbon from GO combustion with metal species, leading to the formation of metal Co and Ni [18]. This was further confirmed by XRD patterns discussed in the next section.

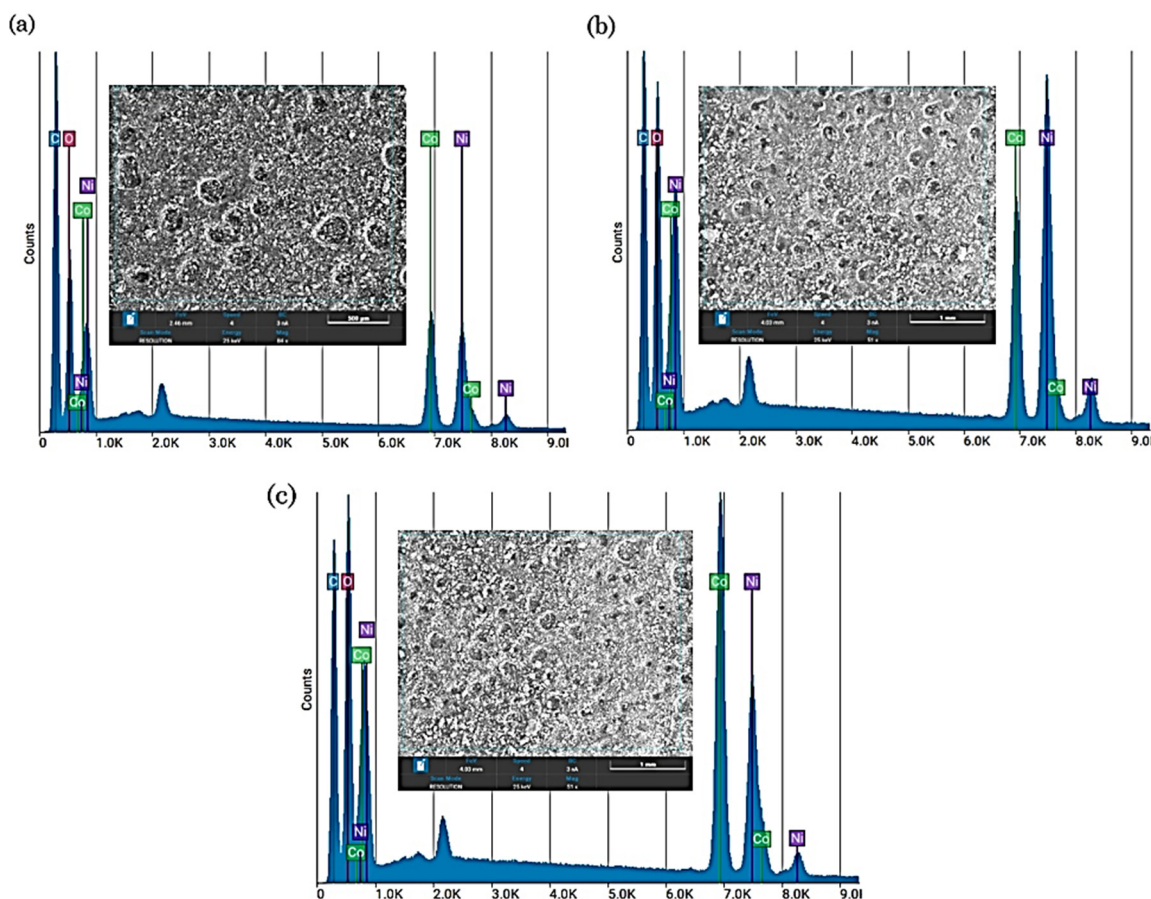


Figure 4. EDX spectra of the fresh (a) 1Co-1Ni/GO; (b) 1Co-2Ni/GO; (c) 2Co-1Ni/GO.

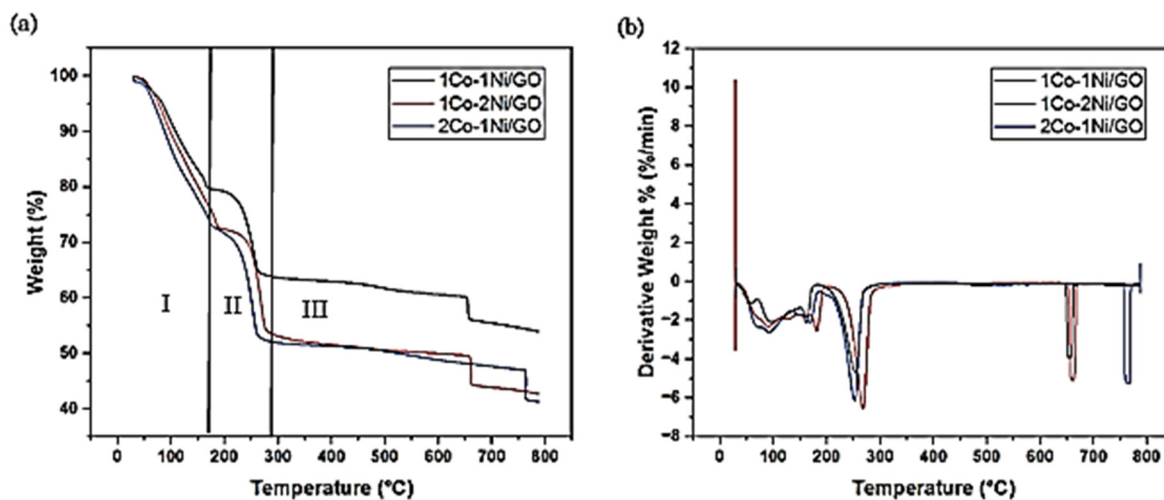
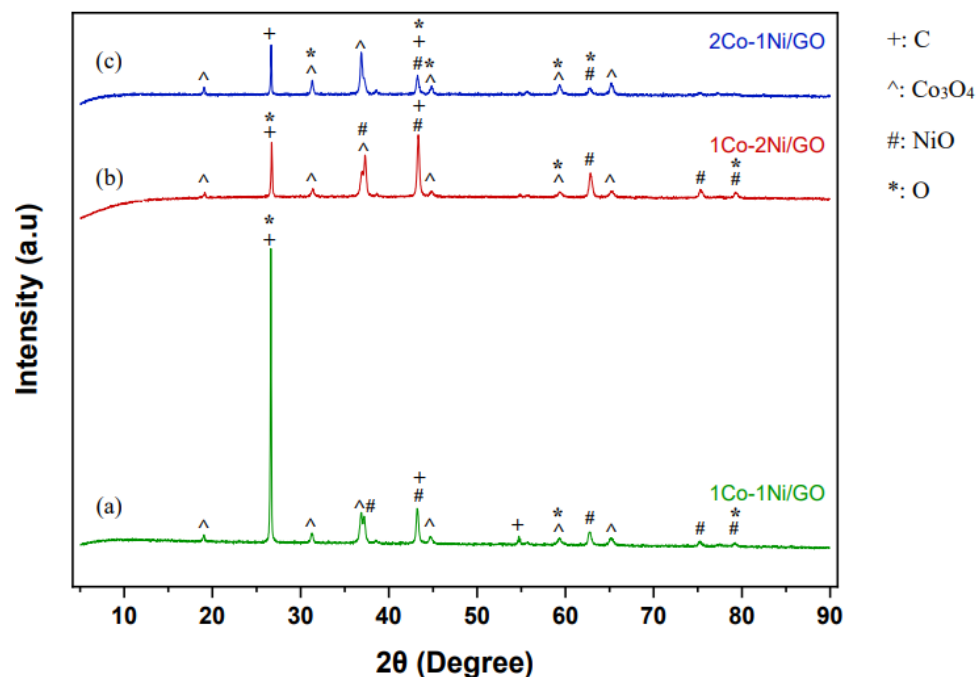


Figure 5. (a) TG and (b) DTG profile of the fresh uncalcined catalysts.

The crystalline phases identified from the bimetallic Co-Ni/GO catalysts are represented by the XRD in Figure 6. All detectable diffraction peaks within the  $2\theta$  range of

5° to 90° were consistent with previous reports and can be indexed to the formation of C (+) and O (\*), which represented GO peaks, cobalt oxide (Co<sub>3</sub>O<sub>4</sub>) (^), and nickel oxide (NiO) (#) [11,22]. Diffraction peaks of sharp intensity were observed, revealing the formation of a well-structured crystalline phase of the catalysts sample. Moreover, the characteristic diffraction peaks of Co and Ni could also be observed in the XRD spectra. These diffractograms were indeed consistent with the presence of elements in the bimetallic Co–Ni/GO catalysts as stipulated by SEM–EDX analysis. Notably, no other impurity phase was detected through XRD analysis.



**Figure 6.** XRD patterns. (a) 1Co-1Ni/GO; (b) 1Co-2Ni/GO; (c) 2Co-1Ni/GO.

The XRD patterns of the catalysts in Figure 6 showed a sharp and tight peak at an average of  $2\theta = 26.62^\circ$ , which corresponded to the diffraction line C, which overlapped with diffraction line O. GO diffraction peaks, which correspond to C and O, can be observed in all patterns at approximately  $2\theta = 26^\circ, 31^\circ, 43^\circ, 54^\circ, 59^\circ, 62^\circ, 65^\circ, 77^\circ,$  and  $79^\circ$ . 1Co-2Ni/GO was expected to consist of more diffractograms of Ni species due to the higher Ni loading compared to Co loading. However, the resulting XRD pattern in Figure 6b showed the opposite. This can be attributed to the smaller intensity of the peaks for NiO compared to that of the Co<sub>3</sub>O<sub>4</sub> due to the small crystallite, resulting in the peaks being not distinguishable. Nevertheless, the detection of Co<sub>3</sub>O<sub>4</sub> and NiO phase signified high interaction between the active metal (Co and Ni) and the support (GO), which was represented by the detection of C and O. Moreover, it can be seen that the diffraction peaks in Figure 6c seemed sharper with increasing Co content, which is an indication that there was an increase in crystallinity by the presence of Co. The obtained results were also in agreement with the N<sub>2</sub> adsorption–desorption analysis, hypothesizing that enhancing the Co loading led to high peak intensity and particle size, finally reducing the surface area. From Table 2, it can be seen that the 2Co-1Ni/GO catalyst displayed a minimum surface area of 9.1568 m<sup>2</sup>/g, in contrast to the other two bimetallic Co–Ni catalysts with lower Co loading.

### 3.2. Catalytic Activity

The catalytic performance of the bimetallic 1Co-1Ni/GO, 1Co-2Ni/GO, and 2Co-1Ni/GO catalysts were evaluated for 5 h TOS at 800 °C in DRM. The activity of the catalysts in the DRM reaction is depicted in Figure 7. At the beginning of the reaction,

high  $\text{CH}_4$  and  $\text{CO}_2$  conversions were obtained from the DRM reaction over the three catalysts. As the reaction progressed, the conversion and yield of the reactants appeared to decrease continuously with TOS for all as-synthesized catalysts. The high  $\text{CH}_4$  conversion observed initially with TOS could be attributed to the synergistic interaction between Co and Ni that may be prominently responsible for the catalytic active role. As the reaction progressed,  $\text{CH}_4$  conversion gradually decreased as there was a gradual deactivation of the active by carbon deposition. However, it is expected that the bimetallic synergy between the Co and Ni mitigated the amount of carbon deposition. Nevertheless, the rate of deposition might outweigh the carbon deposition rate. Generally, in most cases, the conversion of  $\text{CO}_2$  is often higher compared to  $\text{CH}_4$  conversion [37]. This can be attributed to the occurrence of a side reaction, namely RWGS, represented in Equation (2). In the RWGS reaction,  $\text{CO}_2$  and  $\text{H}_2$  reacted to produce CO, resulting in a spiked  $\text{CO}_2$  conversion.

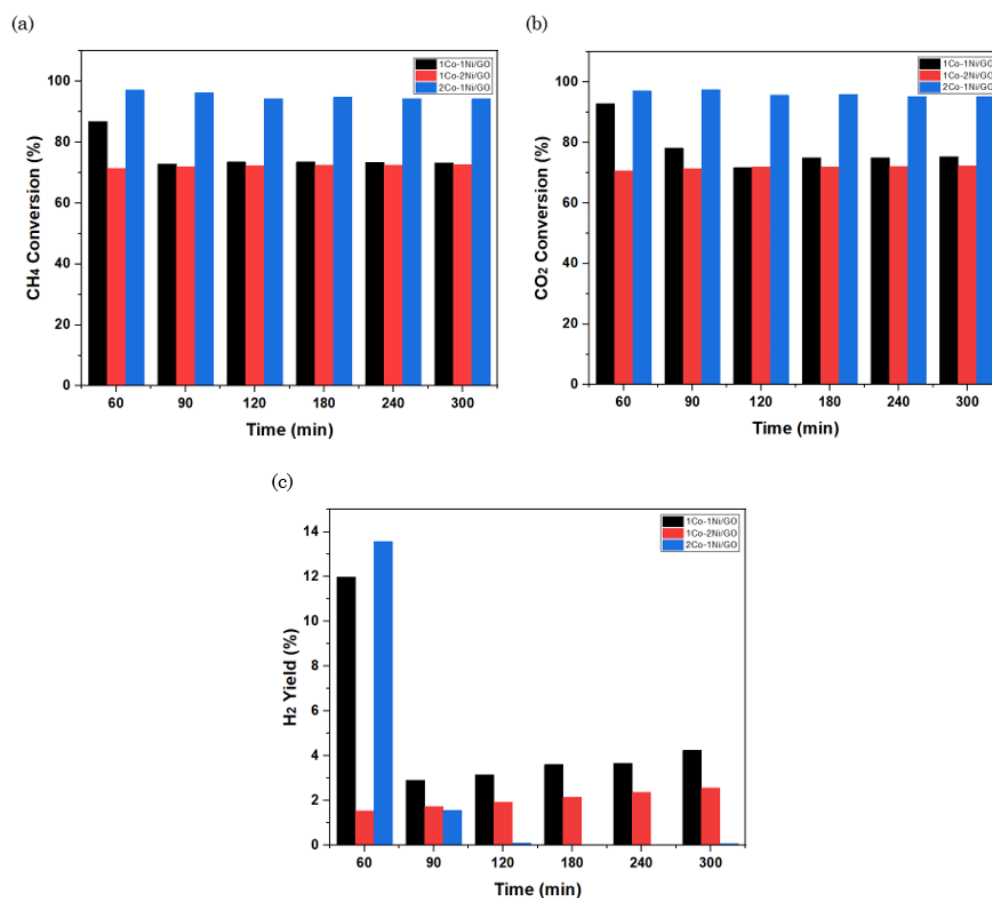


**Figure 7.** Catalytic activity. (a) 1Co-1Ni/GO; (b) 1Co-2Ni/GO; (c) 2Co-1Ni/GO.

As shown in Figure 7c, despite significant conversion attained by all catalysts, as previously discussed, low  $\text{H}_2$  yield was observed from the catalyst activity. This can be attributed to the occurrence of side reactions such as RWGS, CO hydrogenation, and  $\text{CO}_2$  hydrogenation as described in Equations (2), (5) and (6), respectively [38]. These reactions might utilize the  $\text{H}_2$  produced in DRM to produce carbon and carbon monoxide [39]. Furthermore, the carbon formed can significantly reduce the activity of the bimetallic catalyst.

The activity of the bimetallic catalyst as a function of the reactant conversion could be because of the high contents of the Co and Ni and their interaction. However, when compared with Ni, monometallic Co as an active metal catalyst is less active. Consequently, the addition of Co may positively impact the catalytic activity and stability of Ni-based catalysts, forming bimetallic Co-Ni catalysts [40]. The bimetallic 2Co-1Ni/GO catalyst displayed the best performance in terms of activity. The 2Co-1Ni/GO catalyst displayed a high conversion of reactants greater than 90% within 120 min TOS compared to the other

two bimetallic catalysts. Even though the conversion declined afterward, the conversion rate of the 2Co–1Ni/GO catalyst after 4 h remained high and did not show any significant drop. The conversion of CH<sub>4</sub> and CO<sub>2</sub> reached 94.26% and 95.24%, respectively, at 300 min. Additionally, the mesoporosity of the 2Co–1Ni/GO catalyst, which was considerably high, may improve the ability of anti-carbon deposit [41].

#### 4. Conclusions

In this study, a series of bimetallic Co–Ni/GO catalysts were evaluated for the first time in a DRM reaction. The bimetallic with different cobalt and nickel metal loadings were successfully synthesized via the wet-impregnation method. The characterization of the catalysts using N<sub>2</sub> physisorption revealed that the catalysts can be categorized as mesoporous, with 1Co–1Ni/GO being the most mesoporous. The addition of Co slightly decreased the mesoporous properties of 2Co–1Ni/GO but was higher compared to 1Co–2Ni/GO. The SEM–EDX revealed that the metal species were homogeneously distributed on the support, and the results were correlated with XRD analysis. Among the catalysts investigated, the 2Co–1Ni/GO catalyst demonstrated the best activity in the DRM reaction in terms of conversion. The high activity exhibited by cobalt-rich catalyst can be due to its role during methane decomposition. However, the low yield of hydrogen might be due to several side reactions such as reverse water gas reaction, carbon monoxide hydrogenation, and carbon dioxide hydrogenation, which utilize hydrogen produced in the main reaction as a reactant.

Despite the excellent and reasonable catalytic performance of the studied catalysts in terms of CH<sub>4</sub> and CO<sub>2</sub> conversion, the current findings on H<sub>2</sub> yield led to the hypothesis that side reactions were prevalent in catalytic testing. Thus, further research is required to investigate how the side reactions and their undesired products can be suppressed. It is proposed that, in the future, further research may emphasize reaction kinetics and mechanistic studies of DRM over the catalysts, as well as designing and optimizing bimetallic Co–Ni/GO catalysts to help suppress the side reactions.

**Author Contributions:** Conceptualization, B.V.A.; methodology, B.V.A.; software, S.N.S.S.A.B.; validation, B.A., M.S.S., M.A.A. and S.A.; formal analysis, S.N.S.S.A.B. and B.V.A.; investigation, S.N.S.S.A.B.; resources, B.V.A.; data curation, S.N.S.S.A.B. and M.A.A.; writing—original draft preparation, S.N.S.S.A.B.; writing—review and editing, S.N.S.S.A.B. and B.V.A.; visualization, M.S.S., M.A.A., B.A. and S.A.; supervision, B.V.A.; project administration, B.V.A.; funding acquisition, B.V.A. All authors have read and agreed to the published version of the manuscript.

**Funding:** This research was funded by Universiti Teknologi PETRONAS through the STIRF grant (grant number:015LA0-039).

**Data Availability Statement:** No new data were created or analyzed in this study. Data sharing is not applicable to this article.

**Conflicts of Interest:** The authors declare no conflict of interest.

#### References

1. Su, B.; Wang, Y.; Xu, Z.; Han, W.; Jin, H.; Wang, H. Novel Ways for Hydrogen Production Based on Methane Steam and Dry Reforming Integrated with Carbon Capture. *Energy Convers. Manag.* **2022**, *270*, 116199. [[CrossRef](#)]
2. Alipour, Z.; Babu Borugadda, V.; Wang, H.; Dalai, A.K. Syngas Production through Dry Reforming: A Review on Catalysts and Their Materials, Preparation Methods and Reactor Type. *Chem. Eng. J.* **2023**, *452*, 139416. [[CrossRef](#)]
3. Jabbour, K.; El Hassan, N.; Arabi, M.; Chemali, R.; Nasr, Y. A Thermodynamic Methodology toward an Optimized Methane Decomposition Process for Enhanced Hydrogen Production and Low Carbon Accumulation: Effect of Non-Hydrocarbon Co-Feeds. *Chem. Eng. Res. Des.* **2022**, *188*, 50–68. [[CrossRef](#)]
4. Mu, W.-H.; Chasse, G.A.; Fang, D.-C. High Level Ab Initio Exploration on the Conversion of Carbon Dioxide into Oxazolidinones: The Mechanism and Regioselectivity. *J. Phys. Chem. A* **2008**, *112*, 6708–6714. [[CrossRef](#)]
5. Yentekakis, I.V.; Panagiotopoulou, P.; Artemakis, G. A Review of Recent Efforts to Promote Dry Reforming of Methane (DRM) to Syngas Production via Bimetallic Catalyst Formulations. *Appl. Catal. B* **2021**, *296*, 120210. [[CrossRef](#)]
6. Summa, P.; Samojeden, B.; Motak, M. Dry and Steam Reforming of Methane. Comparison and Analysis of Recently Investigated Catalytic Materials. A Short Review. *Pol. J. Chem. Technol.* **2019**, *21*, 31–37. [[CrossRef](#)]

7. Vogt, C.; Kranenborg, J.; Monai, M.; Weckhuysen, B.M. Structure Sensitivity in Steam and Dry Methane Reforming over Nickel: Activity and Carbon Formation. *ACS Catal.* **2020**, *10*, 1428–1438. [[CrossRef](#)]
8. El-Emam, R.S.; Özcan, H. Comprehensive Review on the Techno-Economics of Sustainable Large-Scale Clean Hydrogen Production. *J. Clean. Prod.* **2019**, *220*, 593–609. [[CrossRef](#)]
9. Manna, J.; Jha, P.; Sarkhel, R.; Banerjee, C.; Tripathi, A.K.; Nouni, M.R. Opportunities for Green Hydrogen Production in Petroleum Refining and Ammonia Synthesis Industries in India. *Int. J. Hydrogen Energy* **2021**, *46*, 38212–38231. [[CrossRef](#)]
10. Jang, W.-J.; Jeong, D.-W.; Shim, J.-O.; Kim, H.-M.; Roh, H.-S.; Son, I.H.; Lee, S.J. Combined Steam and Carbon Dioxide Reforming of Methane and Side Reactions: Thermodynamic Equilibrium Analysis and Experimental Application. *Appl. Energy* **2016**, *173*, 80–91. [[CrossRef](#)]
11. Sasson Bitters, J.; He, T.; Nestler, E.; Senanayake, S.D.; Chen, J.G.; Zhang, C. Utilizing Bimetallic Catalysts to Mitigate Coke Formation in Dry Reforming of Methane. *J. Energy Chem.* **2022**, *68*, 124–142. [[CrossRef](#)]
12. Huang, Y.; Li, X.; Zhang, Q.; Vinokurov, V.A.; Huang, W. Carbon Deposition Behaviors in Dry Reforming of CH<sub>4</sub> at Elevated Pressures over Ni/MoCeZr/MgAl<sub>2</sub>O<sub>4</sub>-MgO Catalysts. *Fuel* **2022**, *310*, 122449. [[CrossRef](#)]
13. Yang, B.; Deng, J.; Li, H.; Yan, T.; Zhang, J.; Zhang, D. Coking-Resistant Dry Reforming of Methane over Ni/ $\gamma$ -Al<sub>2</sub>O<sub>3</sub> Catalysts by Rationally Steering Metal-Support Interaction. *iScience* **2021**, *24*, 102747. [[CrossRef](#)] [[PubMed](#)]
14. Ballesteros-Plata, D.; Infantes-Molina, A.; Rodríguez-Castellón, E.; Cauqui, M.A.; Yeste, M.P. Improving Noble Metal Catalytic Activity in the Dry Reforming of Methane by Adding Niobium. *Fuel* **2022**, *308*, 121996. [[CrossRef](#)]
15. Karemore, A.L.; Sinha, R.; Chugh, P.; Vaidya, P.D. Syngas Production by Dry Methane Reforming over Alumina-Supported Noble Metals and Kinetic Studies. *Chem. Eng. Technol.* **2022**, *45*, 907–917. [[CrossRef](#)]
16. Singh, R.; Dhir, A.; Mohapatra, S.K.; Mahla, S.K. Dry Reforming of Methane Using Various Catalysts in the Process: Review. *Biomass Convers. Biorefin.* **2020**, *10*, 567–587. [[CrossRef](#)]
17. Liu, Z.; Zhang, F.; Rui, N.; Li, X.; Lin, L.; Betancourt, L.E.; Su, D.; Xu, W.; Cen, J.; Attenkofer, K.; et al. Highly Active Ceria-Supported Ru Catalyst for the Dry Reforming of Methane: In Situ Identification of Ru $\delta^+$ -Ce<sup>3+</sup> Interactions for Enhanced Conversion. *ACS Catal.* **2019**, *9*, 3349–3359. [[CrossRef](#)]
18. de Araújo Moreira, T.G.; de Carvalho Filho, J.F.S.; Carvalho, Y.; De Almeida, J.M.A.R.; Nothhaft Romano, P.; Falabella Sousa-Aguiar, E. Highly Stable Low Noble Metal Content Rhodium-Based Catalyst for the Dry Reforming of Methane. *Fuel* **2021**, *287*, 119536. [[CrossRef](#)]
19. Wang, F.; Wang, Y.; Zhang, L.; Zhu, J.; Han, B.; Fan, W.; Xu, L.; Yu, H.; Cai, W.; Li, Z.; et al. Performance Enhancement of Methane Dry Reforming Reaction for Syngas Production over Ir/Ce<sub>0.9</sub>La<sub>0.1</sub>O<sub>2</sub>-Nanorods Catalysts. *Catal. Today* **2020**, *355*, 502–511. [[CrossRef](#)]
20. Jiménez, J.D.; Betancourt, L.E.; Danielis, M.; Zhang, H.; Zhang, F.; Orozco, I.; Xu, W.; Llorca, J.; Liu, P.; Trovarelli, A.; et al. Identification of Highly Selective Surface Pathways for Methane Dry Reforming Using Mechanochemical Synthesis of Pd-CeO<sub>2</sub>. *ACS Catal.* **2022**, *12*, 12809–12822. [[CrossRef](#)]
21. Shen, D.; Li, Z.; Shan, J.; Yu, G.; Wang, X.; Zhang, Y.; Liu, C.; Lyu, S.; Li, J.; Li, L. Synergistic Pt-CeO<sub>2</sub> Interface Boosting Low Temperature Dry Reforming of Methane. *Appl. Catal. B* **2022**, *318*, 121809. [[CrossRef](#)]
22. Cai, X.; Hu, Y.H. Advances in Catalytic Conversion of Methane and Carbon Dioxide to Highly Valuable Products. *Energy Sci. Eng.* **2019**, *7*, 4–29. [[CrossRef](#)]
23. Shafiqah, M.-N.N.; Abidin, S.Z.; Roslan, N.A.; Osazuwa, O.U.; Chanakaewsomboon, I. The Synergistic Role of Ni-Co Bimetallic Catalyst for H<sub>2</sub>-Rich Syngas Production via Glycerol Dry Reforming. *J. Energy Inst.* **2022**, *105*, 293–308. [[CrossRef](#)]
24. San-José-Alonso, D.; Juan-Juan, J.; Illán-Gómez, M.J.; Román-Martínez, M.C. Ni, Co and Bimetallic Ni-Co Catalysts for the Dry Reforming of Methane. *Appl. Catal. A Gen.* **2009**, *371*, 54–59. [[CrossRef](#)]
25. Erdogan, B.; Arbag, H.; Yasyerli, N. SBA-15 Supported Mesoporous Ni and Co Catalysts with High Coke Resistance for Dry Reforming of Methane. *Int. J. Hydrogen Energy* **2018**, *43*, 1396–1405. [[CrossRef](#)]
26. Sharifianjazi, F.; Esmaeilkhani, A.; Bazli, L.; Eskandarinezhad, S.; Khaksar, S.; Shafiee, P.; Yusuf, M.; Abdullah, B.; Salahshour, P.; Sadeghi, F. A Review on Recent Advances in Dry Reforming of Methane over Ni- and Co-Based Nanocatalysts. *Int. J. Hydrogen Energy* **2022**, *47*, 42213–42233. [[CrossRef](#)]
27. Horlyck, J.; Lawrey, C.; Lovell, E.C.; Amal, R.; Scott, J. Elucidating the Impact of Ni and Co Loading on the Selectivity of Bimetallic NiCo Catalysts for Dry Reforming of Methane. *Chem. Eng. J.* **2018**, *352*, 572–580. [[CrossRef](#)]
28. Ay, H.; Üner, D. Dry Reforming of Methane over CeO<sub>2</sub> Supported Ni, Co and Ni-Co Catalysts. *Appl. Catal. B* **2015**, *179*, 128–138. [[CrossRef](#)]
29. Zhang, X.; Han, X.; Gao, C.; Wang, X.; Wei, Y.; Zhang, N.; Bao, J.; Xu, N.; He, G. In-Situ Growth of Co/Zn Bimetallic MOF on GO Surface to Prepare GO Supporting Co@C Single-Atom Catalyst for Hg<sup>0</sup> Oxidation. *Fuel* **2023**, *333*, 126135. [[CrossRef](#)]
30. Buttersack, C. Modeling of Type IV and v Sigmoidal Adsorption Isotherms. *Phys. Chem. Chem. Phys.* **2019**, *21*, 5614–5626. [[CrossRef](#)]
31. ZHANG, R.; XIA, G.; LI, M.; WU, Y.; NIE, H.; LI, D. Effect of Support on the Performance of Ni-Based Catalyst in Methane Dry Reforming. *J. Fuel Chem. Technol.* **2015**, *43*, 1359–1365. [[CrossRef](#)]
32. Lyu, L.; Han, Y.; Ma, Q.; Makpal, S.; Sun, J.; Gao, X.; Zhang, J.; Fan, H.; Zhao, T.S. Fabrication of Ni-Based Bimodal Porous Catalyst for Dry Reforming of Methane. *Catalysts* **2020**, *10*, 1220. [[CrossRef](#)]

33. Wang, Y.; Zhang, Y.; Zhao, S.; Zhu, J.; Jin, L.; Hu, H. Preparation of Bimetallic Catalysts Ni-Co and Ni-Fe Supported on Activated Carbon for Methane Decomposition. *Carbon Resour. Convers.* **2020**, *3*, 190–197. [[CrossRef](#)]
34. Yu, I.K.M.; Xiong, X.; Tsang, D.C.W.; Ng, Y.H.; Clark, J.H.; Fan, J.; Zhang, S.; Hu, C.; Ok, Y.S. Graphite Oxide- and Graphene Oxide-Supported Catalysts for Microwave-Assisted Glucose Isomerisation in Water. *Green Chem.* **2019**, *21*, 4341–4353. [[CrossRef](#)]
35. Sharma, S.; Groves, M.N.; Fennell, J.; Soin, N.; Horswell, S.L.; Malardier-Jugroot, C. Carboxyl Group Enhanced CO Tolerant GO Supported Pt Catalysts: DFT and Electrochemical Analysis. *Chem. Mater.* **2014**, *26*, 6142–6151. [[CrossRef](#)]
36. Yu, Y.; Zhang, J.; Chen, C.; He, C.; Miao, J.; Li, H.; Chen, J. Effects of Calcination Temperature on Physicochemical Property and Activity of CuSO<sub>4</sub>/TiO<sub>2</sub> Ammonia-Selective Catalytic Reduction Catalysts. *J. Environ. Sci.* **2020**, *91*, 237–245. [[CrossRef](#)] [[PubMed](#)]
37. Mo, W.; Ma, F.; Ma, Y.; Fan, X. The Optimization of Ni–Al<sub>2</sub>O<sub>3</sub> Catalyst with the Addition of La<sub>2</sub>O<sub>3</sub> for CO<sub>2</sub>–CH<sub>4</sub> Reforming to Produce Syngas. *Int. J. Hydrogen Energy* **2019**, *44*, 24510–24524. [[CrossRef](#)]
38. Cichy, M.; Pańczyk, M.; Słowik, G.; Zawadzki, W.; Borowiecki, T. Ni–Re Alloy Catalysts on Al<sub>2</sub>O<sub>3</sub> for Methane Dry Reforming. *Int. J. Hydrogen Energy* **2022**, *47*, 16528–16543. [[CrossRef](#)]
39. Zhu, L.; Lv, Z.; Huang, X.; Ran, J.; Chen, J.; Qin, C. Understanding the Role of Support Structure in Methane Dry Reforming for Syngas Production. *Fuel* **2022**, *327*, 125163. [[CrossRef](#)]
40. Lyu, L.; Shengene, M.; Ma, Q.; Sun, J.; Gao, X.; Fan, H.; Zhang, J.; Zhao, T.-S. Synergy of Macro-Meso Bimodal Pore and Ni-Co Alloy for Enhanced Stability in Dry Reforming of Methane. *Fuel* **2022**, *310*, 122375. [[CrossRef](#)]
41. Ekeoma, B.C.; Yusuf, M.; Johari, K.; Abdullah, B. Mesoporous Silica Supported Ni-Based Catalysts for Methane Dry Reforming: A Review of Recent Studies. *Int. J. Hydrogen Energy* **2022**, *47*, 41596–41620. [[CrossRef](#)]

**Disclaimer/Publisher’s Note:** The statements, opinions and data contained in all publications are solely those of the individual author(s) and contributor(s) and not of MDPI and/or the editor(s). MDPI and/or the editor(s) disclaim responsibility for any injury to people or property resulting from any ideas, methods, instructions or products referred to in the content.